Optical and Quantum Electronics (2025) 57:497
https://doi.org/10.1007/s11082-025-08409-4

Modification of the structure, optical properties, TGA, and DSC of CMC/polyacrylamide films by CoFe QDs

A. Abou Elfadl[1] · Asmaa M. M. Ibrahim[1] · Adel M. El Sayed[1]

Received: 10 May 2025 / Accepted: 3 August 2025

Abstract
This study employed auto-combustion and solution casting techniques for preparing CoFe QDs and CoFe/carboxymethyl cellulose/polyacrylamide nanocomposite films, respectively. HR-TEM and XRD analyses revealed that CoFe is a polycrystalline material with an *fcc* structure composed of small semi-spherical particles of size < 10 nm. XRD and ATR/FTIR showed the formation of semicrystalline films, where CoFe makes interactions and complexations with the blend functional groups. SEM and EDX analyses showed that the blend is homogeneous with a uniform distribution of CoFe QDs. The blend film showed UV–vis-NIR transmittance up to 71% but decreased with increasing CoFe content. In addition, the indirect (and direct) band gap decreased from 4.8 (5.2) eV to 4.0 eV at 6.0 wt% CoFe QDs. Investigating the thermal properties indicated that CoFe QDs can speed up the blend decomposition through multiple reaction stages. It also confirmed the strong interaction between CoFe and blend chains and decreased the activation energy from 447.9 to 416.8 kJ/mol.

Keywords CoFe quantum dots · Polyacrylamide · Blend and nanocomposites · Thermal analysis · Activation energy · Optical feature

1 Introduction

The worldwide interest in organic (polymer)-inorganic (nanofiller) composite materials increases, owing to their practical applications and contributions to basic science (Pathak et al. 2024). New polymeric materials (combining the advantages of more than one polymer) can be realized via the blending technology, far from the complex and costly chemical approaches (El-Sayed et al. 2011; Sayed et al. 2015; Morsi et al. 2018; Ragab and Rajeh 2020; Elashmawi and Al-Muntaser 2021). Biodegradable, water-soluble polymers (polyethylene oxide (PEO), polyvinyl alcohol (PVA), polyvinylpyrrolidone, polyethylene glycol, polyacrylamide (PAam), carboxymethyl cellulose-sodium salt (CMC-Na), etc.) have chemical diversities essential for multiple practical purposes and follow the restriction of a safe environment (Lefay and Guillaneuf 2023). Among these types, PAam is a linear

✉ A. Abou Elfadl
amh03@fayoum.edu.eg

[1] Faculty of Science, Physics Department, Fayoum University, El-Fayoum 63514, Egypt

biodegradable and amorphous polymer with exceptional hydrophilicity and biocompatibility (Qian et al. 2024). Also, CMC-Na is a smart anionic polyelectrolyte cellulose ether, where β-1, 4-glycosidic bonds connect the repeating units. It is a biodegradable, abundant (cost-effective), and renewable polymer. The repulsion of carboxylate (COO^-) makes the CMC-Na hydrogels highly swell in water (Wang et al. 2023; Wu et al. 2024).

CMC-Na is widely used in the textile and food industries, tissue engineering, water treatment (the removal of textile dyes, heavy metal ions, and pharmaceutical contaminants), and drugs (Wu et al. 2024; Aljeboree et al. 2025). Moreover, this polymer is sensitive to the pH value of the solution or its ionic strength and can be used to amend and enhance the quality of soil (infiltration, water-salt distribution, and crop (wheat/maize) growth in the coastal and alkaline soil) (Li et al. 2024a). The covalent bonds connect the PAam networks, whereas the H bonds connect the networks in CMC-Na. Therefore, combining the two polymers in a blend (PACMC) allows the formation of entanglement points among their networks, avoiding the weak mechanical properties (brittleness) of PAam (Wu et al. 2024). On the other hand, several research groups attempted to boost the multifunctionality of the PACMC blend in industry (wearable electronics and energy-storing applications), water treatment, and agriculture by mixing it with other organic and inorganic compounds.

Qian et al. (Qian et al. 2024) prepared PACMC/LiCl hydrogels with a 2.96 mV/K Seebeck coefficient and 36.51 mS/cm ionic conductivity at room temperature (RT), suitable for thermoelectric supercapacitors. Wu et al. (Wu et al. 2024) prepared PACMC/MXene highly stretchable hydrogels suitable for monitoring human activities (joint bending, performing handwriting recognition, etc.) and wearable electronics. Owing to the function (chemical) groups compatible with both the hydrophilic/hydrophobic feature of Si/C surfaces, the PACMC/styrene-butadiene rubber blend was used to improve the Si@C/graphite anode adhesion, integrity, and cyclability (Yu et al. 2024). Li et al. (Li et al. 2023a) developed a PACMC/tannic acid hydrogel containing $ZnSO_4/MnSO_4$ electrolyte for Zn-ion batteries, serving as a wearable sensing self-powered device. In addition, Xu et al. (Xu et al. 2023) fabricated PVA/PACMC/borax composites for flexible wearable sensors.

Moreover, Wang et al. (Wang et al. 2023) employed the ion imprinting approach to prepare PACMC/Fe_3O_4 magnetic polymer composites for La^{3+} removal/recovery (adsorption/desorption) process from sewage. PACMC blend was also used (to reduce the water evaporation enthalpy) with carbon QDs/MXene (photothermal material) to enhance the evaporation performances of the hydrogel evaporators for freshwater (Jing et al. 2024). Yang et al. (Yang et al. 2024) designed PACMC/ZIF-67 nanocomposites for U (VI) adsorption from seawater, where the carboxyl (COOH) and amino (NH_2) groups in the blend force ZIF-67 to form oriented and penetrating microchannel arrays. Li (Li et al. 2023b) developed Fe^{3+}/PACMC/Ag nanocomposite hydrogel, promising for resistance to infections due to the urinary catheter. Additionally, PACMC copolymer was used for slow urea release to minimize the needed fertilizer dosage and soil contamination (Sultan and Taha 2024).

The nano-sized material (at least one of its dimensions should be < 100 nm) used as fillers can be classified as 0D (nanoparticles and QDs), 1D (nanowires, nanorods, etc.), and 2D (nanosheets, nanobelts, etc.). 2D nanofillers (CuO and Fe_2O_3 nanoplates and GO nanosheets) enhanced the thermal stability and optical features and increased the AC conductivity of the PACMC blend from 21.5×10^{-4} S/m to 24×10^{-4} S/m and boosted its antifungal activities (Abou Elfadl et al. 2023). Among them, the QDs (size < 10 nm) have a higher surface/volume ratio, *i.e.*, they are highly active, and exhibit quantum confinement effects in their electronic and optical characteristics. Therefore, their utilization varies from memories, spintronics, color conversion, optoelectronics, and biomedicine (bioimaging

and biosensing applications related to environmental and biomedical science) (Cotta 2020; Agarwal et al. 2023). CoFe is a magnetic material used in supercapacitors, magnetic recording, and electronic devices (Yang et al. 2014; Kurtan et al. 2020). A few numbers of studies on the CoFe/polymer nanocomposites have been found. According to Kumar et al. (Kumar et al. 2008), incorporating CoFe inside MEH/PPV polymer increased the trap density to 2×10^{18} /cm^3 and decreased the hole mobility to 0.6×10^{-5} cm^2/V·s, valid for light-emitting diode applications. The impact of 0.5 and 1.0 wt% CoFe on the UV–vis parameters and insulation properties of PEO/polymethylmethacrylate nanoparticles was reported (Alanazi and Sayed 2024).

The present study focuses on the preparation of CoFe QDs and CoFe/PACMC polymer nanocomposites to investigate the influence of these 0D fillers on the structural features, UV–vis features, and thermal properties of the blend. HR-TEM, XRD, FTIR, and SEM were utilized to study the structure and morphology of the samples. The results illustrated that CoFe addition improves the UV–vis (optical) and thermal (TGA, DTG, DSC) properties of the PACMC blend for advanced optoelectronics.

2 Materials, preparations, characterization, and measurements

2.1 CoFe QDs preparation

0.5 mol of pure $Co(NO_3)_2.6H_2O$ (molecular weight (M_w) = 291 g·mol^{-1} from Merck), 0.5 mol of $Fe(NO_3)_3.9H_2O$ (M_w = 404 g·mol^{-1} from Merck) and 1.0 mol of $C_6H_8O_7$ (citric acid) (M_w = 192 g·mol^{-1} from PubChem, India) were used to prepare CoFe QDs by the nitrate/citrate auto-combustion route. These amounts were dissolved in 50 mL of ultrapure water (UPW), and ammonia droplets (fuel) were added to the solution to reach pH = 7. The composite solution was dried on a heated plate and then annealed at 550 °C/3.0 h for oxidation and crystallization ($CoFe_2O_4$). The product was then introduced into a tube furnace at 400 °C/2.0 h in the presence of an acetylene stream at normal pressure to obtain CoFe QDs (Wan et al. 2018).

2.2 PACMC and COFe/PACMC film preparation

0.8 g of CMC-Na ($[C_6H_7O_2(OH)_2OCH_2COONa]_n$, supplied by El-Nasr Pharmaceutical Chemicals Co., Egypt) was dissolved in 50 mL of UPW using a bar magnet for stirring/hotplate for 1.0 h/85 °C. Similarly, 0.2 g of PAam ($[CH_2CHCONH_2]_n$, from Tianjin Fu Chen, China) was dissolved in 50 mL UPW at RT. The two solutions were added to each other and stirred for another 1.0 h at RT. The nanocomposite films were prepared by adding x(wt%) = 1.0, 3.0, and 6.0 wt% CoFe to the PACMC blend solution. The weight of CoFe (w_{CoFe}) was determined using the equation $x(\text{wt\%}) = \frac{w_{CoFe}}{w_{CoFe}+w_{PACMC}}$, where w_{PACMC} = 1 g (the total mass of the two polymers), and then dispersed in 15 mL of UPW before mixing with the blend solution. To ensure the uniform distribution of CoFe QDs in the blend, the composite solutions were ultrasonicated for 20 min. The final solutions of blend/composite were cast in Peri-dishes (glass of about 11 cm in diameter) in a leveled plane and left to dry at 40 °C/3 days.

2.3 Devices and measurements

The transmission electron microscopy (JEM-21OO, Joel) operated at 200 kV was employed for investigating the size and morphology of the CoFe prepared by the nitrate/citrate auto-combustion technique. The crystalline phase of CoFe and the film structure were studied by X-ray diffraction (XRD) using a PANalytical's X'Pert/PRO device. The diffractometer employed $Cu_{K\alpha}$ radiation of wavelength (λ) = 0.154 nm. The scan was performed in the 2θ range of 5 – 80°. The film surface morphology, filler distribution, and cross-section (thickness) evaluation were checked by the (Inspect/S/FEI, Holland) scanning electron microscopy. The chemical analyses and elemental mapping were investigated using the energy-dispersive X-ray (EDX) spectroscopy unit attached to the FE-SEM, model QUANTA-200F, SE-BSE. ATR/FTIR (attenuated total reflection/Fourier transform infrared spectra) of the films were collected at RT by using a spectrophotometer (Bruker-vertex-70) in the 4000 – 400 cm^{-1} wavenumber range. UV–vis-NIR optical absorption and transmittance spectra in the λ range of 200 – 1500 nm were recorded using the Shimadzu spectrophotometer UV-3600. The thermal analyses were done using a PerkinElmer/STA/6000. The thermogravimetry (TGA) and differential scanning calorimetry (DSC) were measured at temperatures between 25 and 600 °C at a 10 °C min^{-1} heating rate and a flow of N_2.

3 Results and discussion

3.1 CoFe characterization

An HR-TEM image for the CoFe prepared by the auto-combustion (nitrate/citrate) route is shown in Fig. 1a. The material is composed of small, semi-spherical particles of varying sizes. Due to the small size (high surface/volume ratio) and high surface energy, the particles tend to aggregate into bigger particles; however, their size is less than 10 nm, ensuring the QD-like morphology. Figure 1b is the particle size distribution (histogram), obtained using the ImageJ software, and indicates that the average particle size is about 7.35 nm. Figure 2, the XRD pattern (no. 5) of CoFe QDs, shows that the material is fully crystallized and only two peaks at 44.7° and 65° are detected in the studied 2θ range. These peaks are assigned to (110) and (200) planes. This pattern confirms the formation of CoFe of a body-centred cubic polycrystalline structure. This is consistent with the JCPDS card no. 48–1818 (Yang et al. 2014). The absence of any refractions related to cobalt, iron, and/or their oxides confirms the high purity of CoFe.

The crystallite size of CoFe determined using the well-known Scherrer equation was found to be 10 nm. Figure 1c shows the special area electron diffraction of a single particle (SAED) obtained by HR-TEM. The two white rings are assigned to (110) and (200) reflections, in agreement with XRD results. Yang et al. (Yang et al. 2014) prepared CoFe nanoparticles 75 nm in size by the thermal reduction of a layered double hydroxide material at 450 °C in N_2/H_2 gas. The electrospun CoFe/carbon nanofiber electrode, prepared at 280 – 800 °C for supercapacitor applications, showed a mean size (diameter) of about 0.243 µm (Kurtan et al. 2020). These data revealed that the nitrate/citrate auto-combustion technique is facile, energy-saving, and effective for obtaining CoFe of QD morphology.

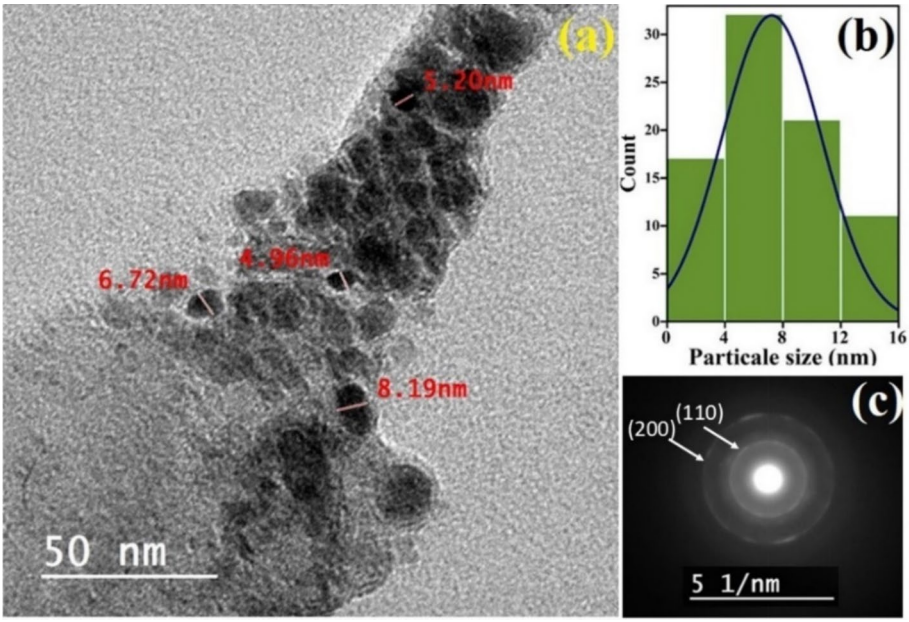

Fig. 1 (**a**) HR-TEM image for CoFe, (**b**) histogram of particle size distribution, and (c) SAED for a single CoFe particle

3.2 Structural properties of the nanocomposite (CoFe/PACMC) films

Figure 2 shows the XRD patterns of PACMC and CoFe/PACMC composites. The broad peak in the 2θ range of 17–30° (centered at ~ 21°) arises due to regular carbon (C) chains in the PACMC blend (Yang et al. 2024). The other two minor reflections at 32° and 49° are also present in this pattern. Similar reflections were noticed in the PACMC blend modified with activated C and $CaCl_2$ (Aljeboree et al. 2025). According to Morsi et al. (Morsi et al. 2018, 2021), CMC-Na exhibits its main XRD peak at 2θ = 21°, and PAam exhibits a wide halo around 2θ = 23°. Sultan and Taha found that the reflections of CMC are at 20°, 31.5°, and 45.35° (Sultan and Taha 2024). These results indicate that the semi-crystallinity of the blend comes from the CMC-Na structure. The composite films show similar patterns with some differences: *i*) the main diffraction peak becomes narrower and less intense, especially at CoFe content of 1.0 wt%. Thus, loading CoFe QDs encourages the formation of more amorphous regions, i.e., deteriorates the film crystallinity. *ii*) The center of this peak is right-shifted (moved to a higher 2θ value). This means a decrease of the *d*-spacing (according to Bragg's law: $d \propto \frac{1}{\sin\theta}$), and compacted films. *iii*) The (110) reflection of CoFe is seen (at the same 2θ value of 44.7°) in the patterns of composite films with increased intensity as the CoFe content increases. Points *ii* and *iii* confirm the presence and interaction of CoFe with the blend chains of the composite films and the ability of CoFe to modify the blend structure, maintaining its cubic crystal structure.

Figure 3a, b shows the surface morphology of PACMC blend loaded with 1.0 and 6.0 wt% CoFe QDs. The insets show a cross-sectional view, film thickness, and a part of the film surface near the cross-section. This figure shows a homogeneous surface, indicating the compatibility between CMC-Na and PAam in the blend. The CoFe QDs are uniformly

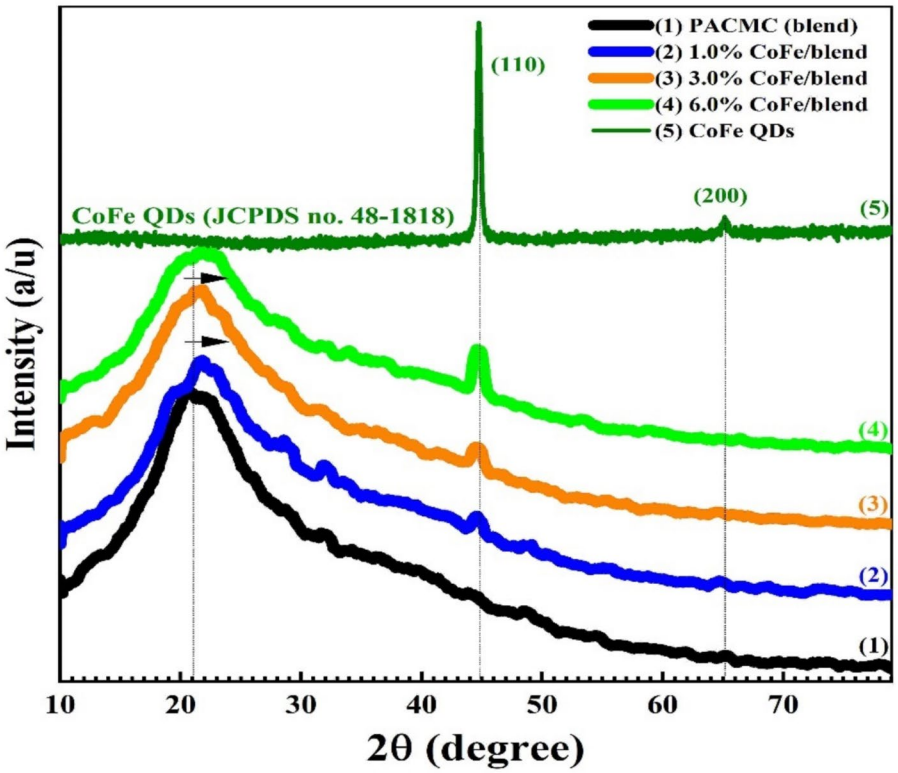

Fig. 2 XRD patterns of CoFe QDs, PACMC blend, and CoFe/blend nanocomposites

distributed on the surface, with some agglomeration at 6.0 wt% content due to the high surface energy of these QDs. The average thickness of the 1.0 wt% and 6.0 wt% CoFe/PACMC films is about 46.3 and 44.86 µm, which are almost the same.

3.3 The chemical analyses and FTIR spectroscopy

Figure 4 shows the EDX analysis of the CoFe sample. The peaks of the Fe element appear at 0.7, 6.4, and 7.05 keV, representing the L_{α}, K_{α}, and K_{β} emission lines, respectively. While the emission lines of Co (L_{α}, K_{α}, and K_{β}) are seen at 0.77, 6.93, and 7.65 keV. The inset table shows that the atomic percentage of Fe: Co is 96.65:3.35%, but both Fe and Co are uniformly distributed, as seen in the inset image. There is a minor peak at 0.27 keV arising from the used grid. In addition, a small peak at 0.5 keV indicates the presence of O. This may indicate the existence of the $CoFe_2O_4$ phase, but below the detection limit of the XRD technique.

Figure 5a shows the EDX spectrum of the 6.0 wt% CoFe/PACMC nanocomposite film. The Kα emission lines of C, N, O, and Na, which are the main components of the blend, appear at 0.28, 0.4, 0.52, and 1.04 keV, respectively. Moreover, the Fe and Co elements are seen at the same position in Fig. 4. This result is consistent with XRD results. The scanned area of the films is shown in Fig. 5b, where the high surface energy of the CoFe QDs forces

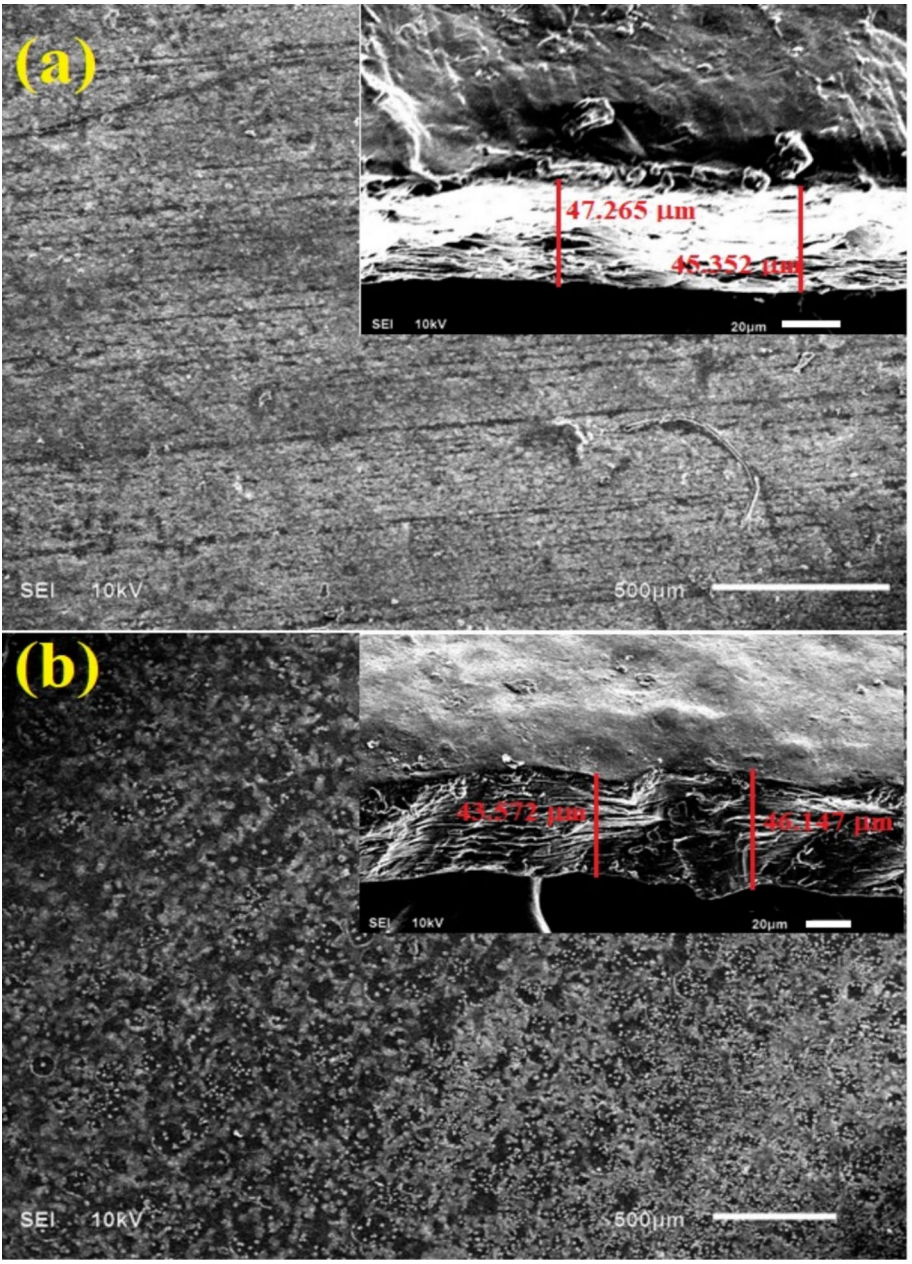

Fig. 3 **(a**, **b)** SEM (top view) and the cross-sectional view and film thickness (insets) of 1.0 and 6.0% CoFe QDs/blend nanocomposite films

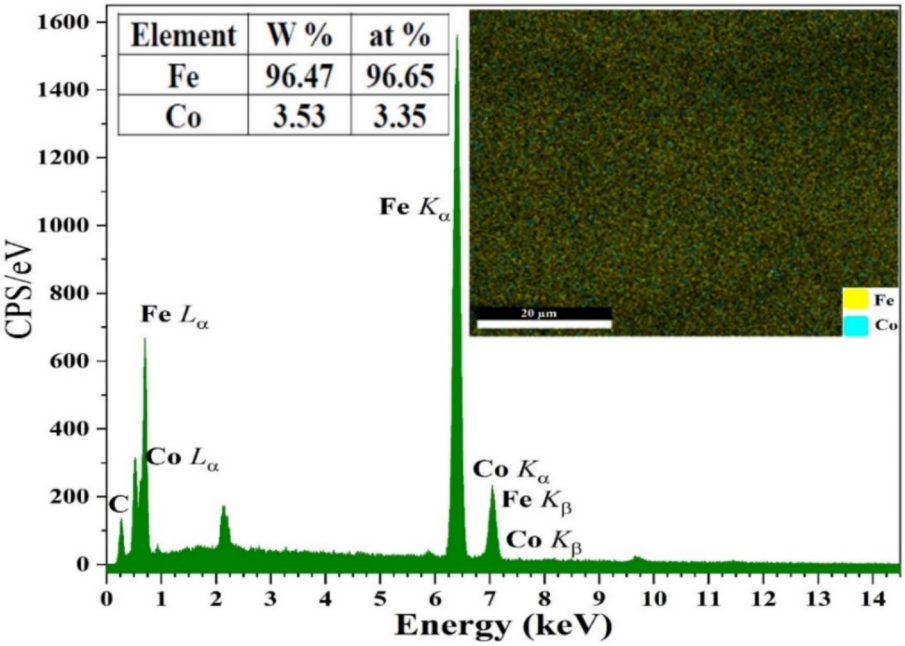

Fig. 4 EDX analysis of CoFe QDs. The inset table shows the Fe/Co ratio, and the inset image shows the Fe and Co mapping

these particles to agglomerate. This tendency is clear in Fig. 5c, where CoFe QDs are accumulated at some position in higher concentration.

The attenuated total reflection (ATR)-Fourier transform infrared (FTIR) spectra of the blend and CoFe/PACMC films are shown in Fig. 6. The spectrum (transmittance mode) of PACMC blend shows a broad band in the higher wavenumber region that seems to be two adjacent and overlapped bands, one centered at 3345 cm^{-1} and can be assigned to the vibration of –NH of PAA (stretching mode), and the other centered at 3192 cm^{-1} and can be assigned to the vibration of OH of CMC (stretching mode) (Aljeboree et al. 2025). The stretching vibration of –NH in PAam generally occurs at higher energies (3500 and 3400 cm^{-1} (El-Gamal and Sayed 2019)). Here, the shift of the –NH band to lower frequencies (3345 cm^{-1}) is owing to the formation of entanglement points between CMC-Na and PAam networks due to the interaction of H bonds in the first polymer with the covalent bonds in the second one (Wu et al. 2024). The intensity (depth) of these overlapped bands decreases with increasing CoFe content. The spectrum also shows the asymmetric-symmetric C–H vibrations in the CMC-Na and PAam backbone at 2930–2860 cm^{-1} (Li et al. 2023b; Sultan and Taha 2024). The intensity of these two bands gradually diminishes with increasing CoFe QDs content. Oppositely, the C–H band intensity increased upon loading Fe_3O_4 200–300 nm in size (Wang et al. 2023). The band at about 2355 cm^{-1} is assigned to C–N vibration (Roheen et al. 2024), where its intensity increases with CoFe content.

The C = O of CMC-Na and PAam vibrates strongly at 1655 cm^{-1}. Yang et al. (Yang et al. 2024) detected this stretching vibration at 1674 cm^{-1}. The asymmetric/symmetric stretch of COO^-(CMC-Na) is seen at 1583/1410 cm^{-1} (Wu et al. 2024). The two peaks around 1600 cm^{-1} in the blend shifted by about 4 cm^{-1} to higher frequencies after loading CoFe QDs, indicating the complexation between COO^- and CoFe QDs (Li et al. 2023b).

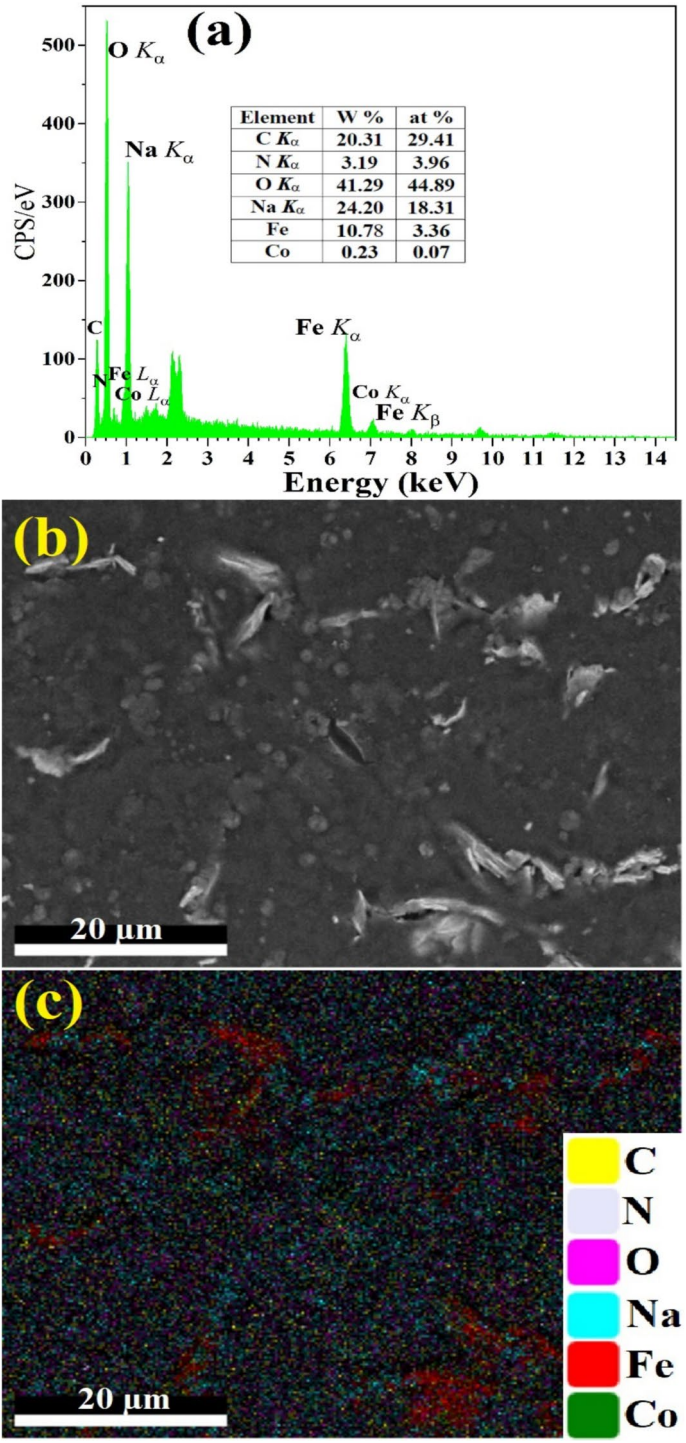

Fig. 5 eZAF smart quant results: (**a**) EDX analysis of 6.0 wt% CoFe/PACMC, (**b**) the investigated area, and (**c**) the elemental mapping

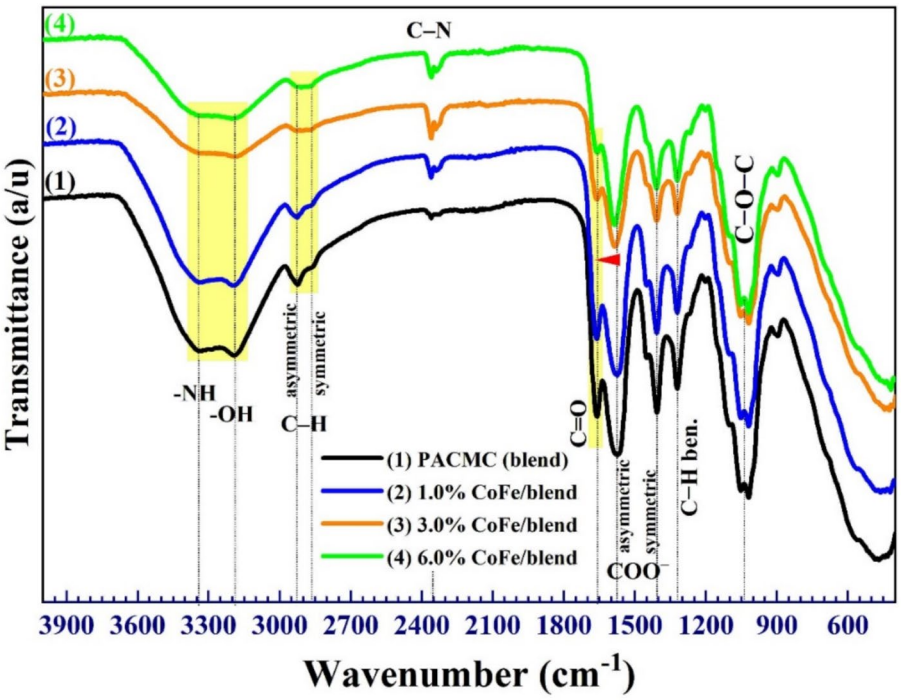

Fig. 6 ATR/FTIR spectra of PACMC blend and CoFe/blend nanocomposites. The red arrow shows the peak shift

The C – H vibration (bending mode) appears at 1320 cm^{-1} (Wu et al. 2024). The band at 1020 – 1050 cm^{-1} is assigned to the stretching vibrations of –C–O–C– (ether) groups. This high intensity and sharpness of this band arise because of the abundance of C – O – C groups in the CMC, which is the major component (80%) of the PACMC blend. The shoulder at 1098 cm^{-1} may be assigned to the CH–O–CH_2 vibration resulting from the interaction between the OH group in the hydroglucose (CMC-Na) and the π bond of PAam (Sultan and Taha 2024). The decrease in the intensity of most of the bands with increasing CoFe content means a restriction for the PACMC blend functional groups to vibrate, owing to the H bonding between Co and/or Fe, and indicates that CoFe QDs reinforce PACMC (Alanazi and Sayed 2024).

3.4 UV–vis study

Figure 7a shows that the transmittance of PACMC blend in the visible and IR spectral ranges ($\lambda \geq 380$ nm) is in the range of 54–71%. This range decreases with doping to 10–45% at 6.0 wt% CoFe QDs. At this ratio, a small portion of UV photons can transmit. This means CoFe QDs can be used to block UV light in these nanocomposite films. 1.0 wt% CoFe/PACMC exhibits 44–68% transmittance, and this range is suitable for some optoelectronic applications (Abou Elfadl et al. 2023). The absorption edge moved to higher λ with increasing CoFe content, revealing a change in the bandgap.

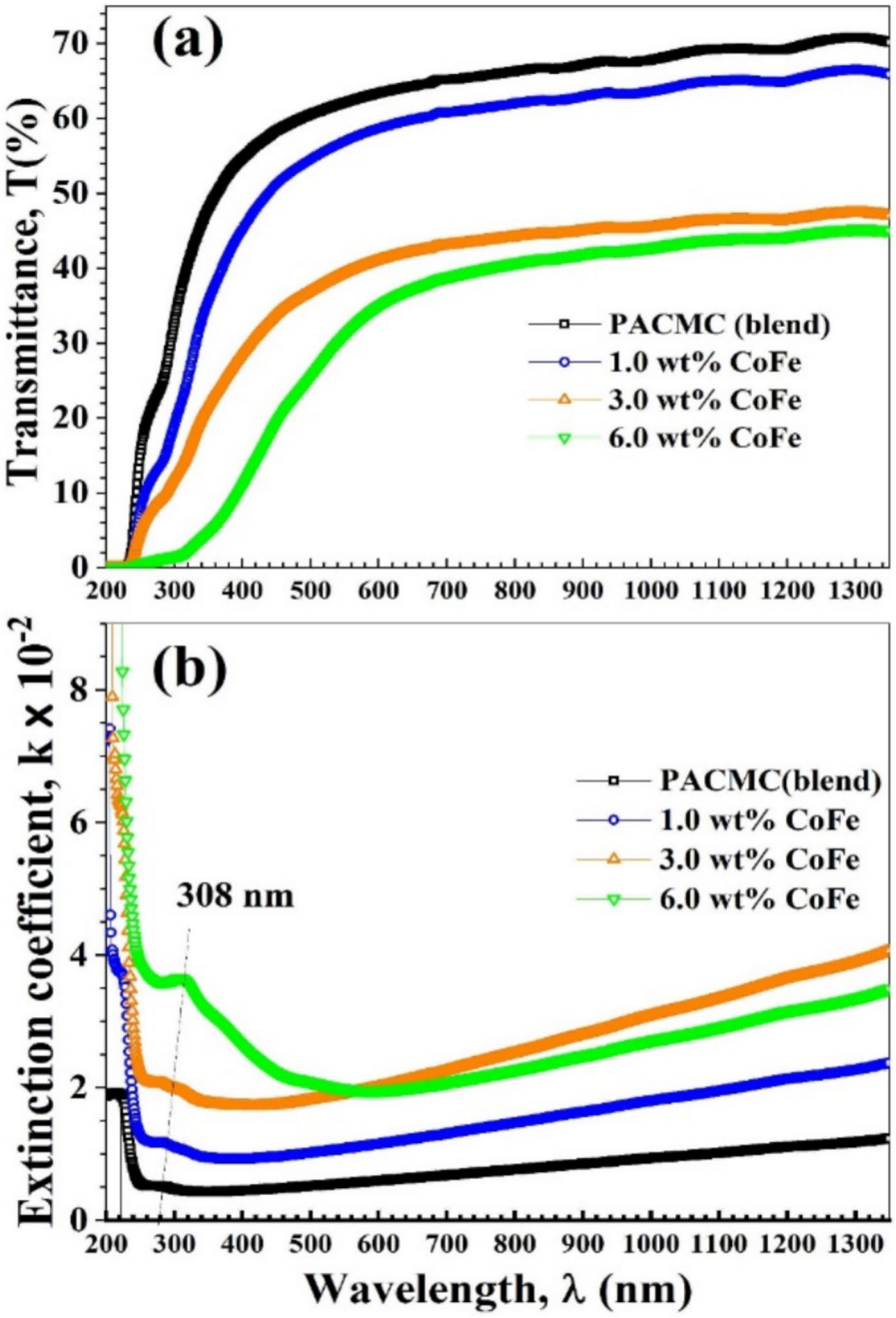

Fig. 7 **a**, **b** Influence of CoFe QDs loading (1.0, 3.0 and 6.0%) on the transmittance and extinction coefficient of PACMC films

Figure 7b displays the extinction coefficient (k) of the films in the studied λ range. The k parameter $\left(k = \frac{2.303\times \text{Absorbance}\times\lambda}{4\pi}\right)$ represents the lost part (via the events of scattering and absorption) of the electromagnetic photons in the films. The films have k values in the range of $(1.25–4.75)\times10^{-2}$, where k increases significantly with the rise of the CoFe QDs content from 1.0 to 6.0 wt%. The band at 220 nm in the k spectra of PACMC and the blend loaded with 1.0 wt% CoFe can be assigned to the $n\rightarrow\pi^*$ transitions. This band arises due to the existence of C=O (unsaturated) group in CMC-Na and PAam polymers, which is consistent with FTIR results, where this band was detected at 1665 cm^{-1} (Fig. 6) (Morsi et al. 2022; Abdallah et al. 2022). We can observe another band at 280 nm, which enhances gradually with CoFe loading and shifts to 308 nm at 6.0 wt% CoFe QDs content. This band can be assigned to the $\pi\rightarrow\pi^*$ transitions, and the possibility of CoFe QDs to form charge transfer complexes with the PACMC functional groups (Elashmawi and Al-Muntaser 2021). The linear increase of k values in the IR spectral range indicates that CoFe/PACMC films can be employed for IR sensing applications.

The impact of CoFe QDs on the band structure of PACMC can be evaluated by determining the indirect and direct optical band gaps (E_g^{ind}&E_g^{dir}) of the films using Tauc's relation (Fewaty et al. 2016): $(\alpha h\upsilon)^{1/r} = A(h\upsilon - E_g)$, where $h\upsilon$ is the energy of incident photons in eV, A is a constant, and $r=2$ or $\frac{1}{2}$ for indirect allowed (E_g^{ind}) and direct allowed transitions (E_g^{dir}), respectively. Figure 8a, b shows the $(\alpha h\upsilon)^{1/2}$ and $(\alpha h\upsilon)^2$ against $h\upsilon$. According to Tuac's model, the E_g^{ind} and E_g^{dir} are obtained by extrapolating straight-line parts in the plots to meet the x-axis. The $E_g^{ind}(E_g^{dir})$ of the blend is 4.8 (5.2) eV, decreased to 4.6 (5.02) eV, 4.5 (4.8) eV, and 4.0 eV upon loading 1.0, 3.0, and 6.0 wt% CoFe QDs. XRD results indicated a decrease in the crystallinity index of the films, where the introduced CoFe QDs increased the disordered state in the films. The loaded QDs may form conductive networks and ways for the movement of charge carriers from the valence to the conduction bands, resulting in the observed band gap reduction (Abdallah et al. 2022). A similar finding was reported for PACMC modified with CuO nanopaltes, where the E_g^{ind} and E_g^{dir} decreased from 4.8 (5.5) eV to 3.6 (4.1) eV (Abou Elfadl et al. 2023). In our work (CMC-Na (80%)/PAam (20%) shows E_g^{ind} and E_g^{dir} are similar to those of the same blends but with different ratios. The E_g^{ind} (E_g^{dir}) of CMC-Na (75%)/PAam (25%) and CMC-Na (50%)/PAam (50%) were found to be equal to 4.90 (5.27) eV (Awad et al. 2020), and 4.97 (5.38) eV (Elashmawi and Al-Muntaser 2021), and were also reduced by loading carbon nanotubes or CuO nanoparticles.

3.5 TGA and DSC (thermal analysis) thermograms

Figure 9a, b displays the weight loss (W%) (thermal gravimetric; TG), and weight loss rate (differential thermal gravimetric; DTG) of PACMC blend and CoFe/blend nanocomposites as a function of temperature from RT to 600 °C. The TG curves evidence the presence of a three-stage decomposition process. For PACMC blend, the first stage occurring between RT and 260 °C can be divided into two parts: i) from RT to 150 °C, the W% is about 10.5% (the remaining weight is 89.5%), and is due to the evaporation of water. ii) from 150 to 260 °C, where the rate of W% is smaller and reaches about 18%. The second decomposition stage between 260 and 310 °C is the main decomposition process. Such a stage is attributed to the glycoside linkages and breakdown of the carboxymethyl cellulose backbone (Aljeboree et al. 2025). In the third stage between

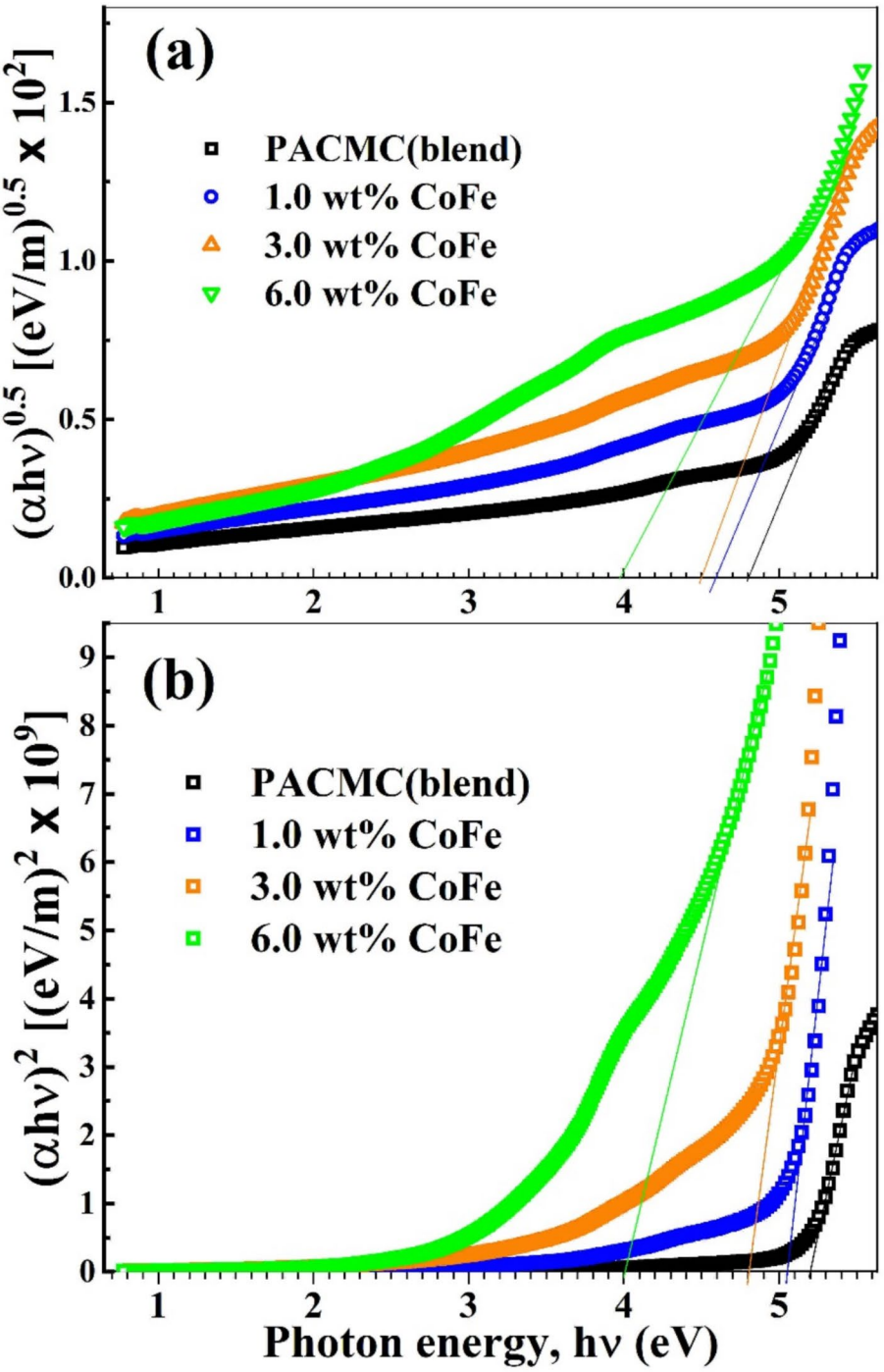

Fig. 8 **a**, **b** Decrement of the indirect and direct E_g of PACMC films with loading 1.0, 3.0, and 6.0% CoFe QDs

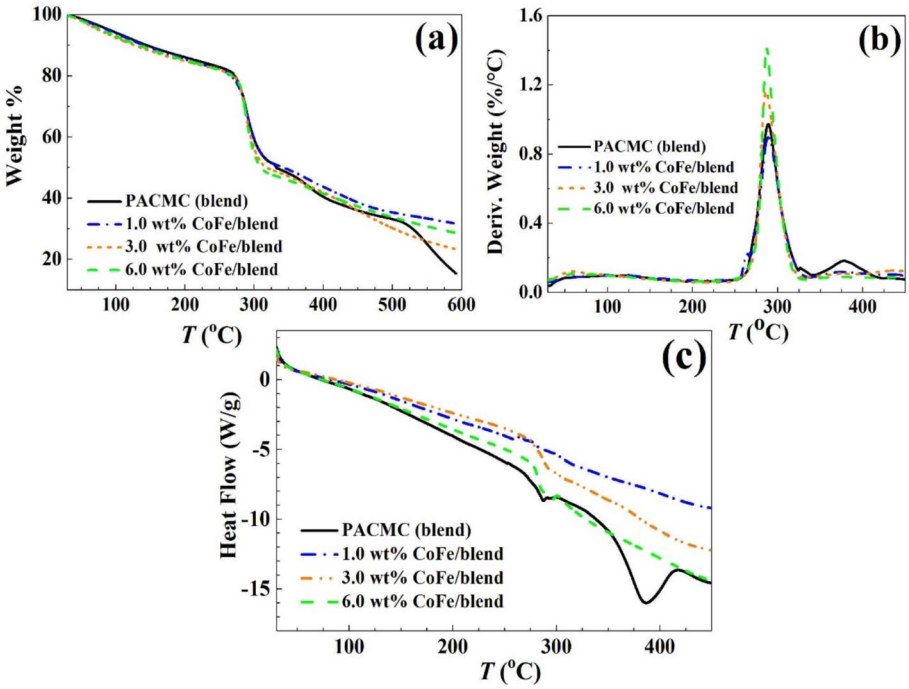

Fig. 9 (**a**) TG, (**b**) DTG, and (**c**) DSC thermograms for PACMC blend and CoFe/blend nanocomposites

310 and 500 °C, the loss W% moves gradually from 45% (remaining weight is 55%) to 67% and is attributed to CO_2 removal (disposal) from the blend structure (Aljeboree et al. 2025) and the pyrolysis of carbonaceous (Li et al. 2018) as well as the PAam's main chain scission and the imide group breakdown (Li et al. 2024b; Steudel et al. 2019). At T = 600 °C, 15% remaining weight represents the mass of char. TG curves of CoFe/blend nanocomposites exhibit almost the same decomposition profiles. Between 30 and 260 °C, W% is associated with the release of water. In the second stage, the W% increases with increasing CoFe content. In addition, the slope of the TG curves is steeper than that of the blend, suggesting that the CoFe QDs accelerate the decomposition of the PACMC blend, i.e., CoFe QDs metal promotes the catalytic decomposition of the PACMC blend on heating (Wang et al. 2016, 2017). Furthermore, the char yield of CoFe/PACMC nanocomposites is greater than that of PACMC blend. Li et al. revealed that ZnO QDs decrease the thermal decomposition rate of CMC (Li et al. 2018).

DTG curves (Fig. 9b) show that the decomposition of PACMC (blend) and its CoFe nanocomposites comprises at least four processes in addition to the evaporation of water, confirming the existence of multiple reaction stages during thermal decomposition. The third weight loss can be divided into two weight losses appearing as two intense overlapping signals, a peak accompanied by a shoulder at higher temperatures. The intensity of the low-temperature peak diminishes from 0.19 to 0.08 at the expense of the high-temperature shoulder with increasing the CoFe content from 1.0 to 6.0 wt%.

The thermal stability was assessed based on the initial decomposition temperature (T_{2i}), maximum weight loss temperature (T_{2max}), and maximum weight loss rate

Table 1 Thermal properties of PACMC (blend) and CoFe/blend nanocomposites in the 2nd decomposition stage: Maximum decomposition temperature T_{2max}, maximum weight loss rate (DTG $_{2max}$), the initial temperature of decomposition T_{2i}, and the activation energy E_{2a}

Sample	T_{2max}(°C)	DTG $_{2max}$ %/°C	T_{2i}(°C)	E_{2a}(kJ/mol)
PACMC (blend)	289.0	0.97	276.5	447.9
1.0 wt% CoFe /blend	288.9	0.90	275.9	427.9
3.0 wt% CoFe /blend	287.4	1.16	277.3	424.9
6.0 wt% CoFe /blend	286.7	1.41	280.0	416.8

(DTG_{2max}) of the second decomposition stage; these parameters are determined and listed in Table 1. As evident in Fig. 9b and Table 1, concerning the PACMC blend, CoFe/blend nanocomposites are characterized by a narrower decomposition temperature range and lower T_{2max}. On the other hand, the nanocomposite samples are characterized by higher T_{2i} compared to PACMC (276.5 °C). Moreover, the maximum weight loss rate increases with increasing the CoFe QD content. The DTG curve of 6.0 wt% CoFe/blend showed the lowest T_{2max} at 286.6 °C compared to PACMC blend at 289.1 °C. The decreased T_{2max} reveals that the presence of CoFe affects the molecular structure and bonding energy of PACMC blend, which perturbs the physical (van der Waals) interactions between the PACMC chains and degrades the blend stability (Mahmoud and Al-Ghamdi 2010). In addition, the XRD results showed that the addition of CoFe increases the amorphous regions of PACMC, which increases the flexibility of the PACMC chains, thus reducing its thermal stability.

The impact of the CoFe QD on the thermal stability of the PACMC blend was confirmed by assessing the energy of activation of the second decomposition (E_{2a}) by applying Coats–Redfern's formula (Coats and Redfern 1964):

$$\ln\left[\frac{-\ln(1-\mu)}{T^2}\right] = -\frac{E_{2a}}{RT} + \ln\left[\frac{BR}{\gamma E_{2a}}\left(1-\frac{2RT}{E_{2a}}\right)\right] \quad (1)$$

where μ, B, T, t, R, and γ are the decomposition fraction, the pre-exponential factor(s^{-1}), the temperature (K), the time (min), the universal (general) gas constant, and the heating rate, respectively. The second term in the RHS of Eq. 1 can be reduced to: $\ln\left[\frac{BR}{\gamma E_{2a}}\right]$ as $\left(\frac{2RT}{E_{2a}}\right)$ is much less than 1. The plot of $\ln\left[\frac{-\ln(1-\mu)}{T^2}\right]$ versus T^{-1} gives a straight line with slope equal to $-E_{2a}\ R^{-1}$. Table 1 shows that the E_{2a} value decreases with increasing CoFe content, even though the T_{2i} increased, which indicates a significant catalytic effect of CoFe QDs in this process. The lower energy of activation of nanocomposites illustrates their lower stability compared with the PACMC.

The thermal behaviour was further studied through the DSC analysis to evaluate the reaction heat of the decomposition processes of the samples. The DSC curve of the PACMC blend reveals a very broad endothermic peak followed by two exothermic peaks (Fig. 9c), without discernible glass transition temperatures (T_g) in the DSC curves of the PACMC blend and nanocomposite films. Similarly, the DSC curves of GO/MWCNTs/chitosan/PEO (Ibrahim et al. 2023) and CuO/PVC nanocomposites (Alshamari et al. 2025) showed no evidence of T_g. The endotherm extended to 160 °C with a peak temperature of 127.5 °C, referring to the loss of water and absorbed energy of 67.2 J/g. However, the exothermic peaks with temperature maxima at 287.4 and 385.3 °C and energy release of

88.1 and 733.2 J/g, respectively, are related to the decomposition of the blend, namely the 2nd and 3rd stages. No significant change in the endothermic peak position was observed upon the incorporation of CoFe, however, the absorbed heat of reaction reduced to 31.7 J/g for 6.0 wt% CoFe QDs content. On the other hand, the addition of CoFe complicated the decomposition exothermic peaks of the PACMC blend that appeared as a peak overlapped with a shoulder, which reflects the strong interaction between CoFe and blend chains. The first energy release was reduced to 38.7 and 87.1 J/g for 3.0 and 6.0 wt% CoFe content, respectively.

4 Conclusion

Semi-spherical CoFe particles, 7.35 nm in size and *fcc* structure, were prepared by an auto-combustion route and incorporated into CMC/polyacrylamide films through solution casting. XRD results showed the semicrystalline structure of the blend and that CoFe made the films more compact. SEM showed the surface homogeneity of the blend and the uniform distribution of CoFe QDs. FTIR showed the reinforcing effect of CoFe towards restricting the vibrations of the blend's functional groups due to the H-bond formation with Co and Fe. CoFe QDs limited the UV–visible transmittance of the blend and improved the linear absorption in the IR spectral range, indicating the suitability of films for shielding the UV light and for IR sensing applications. The semiconducting nature of the blend was also improved, where CoFe incorporation narrowed the E_g^{ind} or E_g^{dir} of the blend from 4.8 or 5.2 eV to 4.0 eV. The TG analysis showed a three-stage decomposition process and speeding up with CoFe QDs. DTG curves showed multiple reaction stages during the decomposition. The T_{2i}, T_{2max}, and DTG_{2max} values revealed that the blend's thermal stability was affected by CoFe content, and the E_a value decreased. The absorbed energy of 67.2 J/g was reduced to 31.7 J/g at 6.0 wt% CoFe QDs content. DSC confirmed the strong interaction between CoFe and blend chains and that the first energy release decreased from 88.1 to 38.7 and 87.1 J/g for 3.0 and 6.0 wt% CoFe content, respectively. The findings indicate that CoFe/PACMC nanocomposites are the best candidate materials with reasonable thermal stability for optoelectronics requiring VU shielding and IR sensors.

Author contributions The three authors A. Abou Elfadl, Asmaa M. M. Ibrahim, Adel M. El Sayed contributed equally in all parts of this submission.

Funding Open access funding provided by The Science, Technology & Innovation Funding Authority (STDF) in cooperation with The Egyptian Knowledge Bank (EKB).

Data Availability No datasets were generated or analysed during the current study.

Declarations

Conflict of interest The authors declare no competing interests.

5. References

Abdallah, E.M., Morsi, M.A., Asnag, G.M., Tarabiah, A.E.: Structural, optical, thermal, and dielectric properties of carboxymethyl cellulose/sodium alginate blend/lithium titanium oxide nanoparticles: biocomposites for lithium-ion batteries applications. Int. J. Energy Res. **46**, 10741–10757 (2022). https://doi.org/10.1002/er.7877

Abou Elfadl, A., Ibrahim, A.M.M., El Sayed, A.M., Saber, S., Elnaggar, S., Ibrahim, I.M.: Influence of α-Fe_2O_3, CuO and GO 2D nano-fillers on the structure, physical properties and antifungal activity of Na-CMC–PAAm blend. Sci. Rep. **13**, 12358 (2023). https://doi.org/10.1038/s41598-023-39056-y

Agarwal, K., Rai, H., Mondal, S.: Quantum dots: an overview of synthesis, properties, and applications. Mater. Res. Express **10**, 062001 (2023). https://doi.org/10.1088/2053-1591/acda17

Alanazi, T.I., El Sayed, A.M.: Reinforcing the structure, optical, and dielectric spectroscopies of poly(ethylene oxide)/poly(methyl methacrylate) thermoplastics by CoFe nanoparticles for optoelectronic device fabrication. Opt. Quantum Electron. **56**, 1224 (2024). https://doi.org/10.1007/s11082-024-07113-z

Aljeboree, A.M., Ghazi, H.H., Hussein, S.A., Jawad, M.A., Khuder, S.A., Alkaim, A.F.: Facile fabrication of a low-cost carboxymethyl cellulose–polyacrylamide composite for the highly efficient removal of cationic dye: optimization, kinetic and reusability. J. Iran. Chem. Soc. **22**, 91–111 (2025). https://doi.org/10.1007/s13738-024-03132-5

Alshamari, A., El Sayed, A.M., Taha, S.: Developing thermally stable CuO/DPC/PVC nanocomposite films for flexible UV shielding and dielectric applications. J. Mol. Struct. **1343**, 142893 (2025). https://doi.org/10.1016/j.molstruc.2025.142893

Awad, S., El-Gamal, S., El Sayed, A.M., Abdel-Hady, E.E.: Characterization, optical, and nanoscale free volume properties of Na-CMC/PAM/CNT nanocomposites. Polym. Adv. Technol. **31**(1), 114–125 (2020). https://doi.org/10.1002/pat.4753

Coats, A.W., Redfern, J.: Kinetic parameters from thermogravimetric data. Nature **201**, 68–69 (1964). https://doi.org/10.1038/201068a0

Cotta, Mônica.A.: Quantum dots and their applications: what lies ahead? ACS Appl. Nano Mater. **3**(6), 4920–4924 (2020). https://doi.org/10.1021/acsanm.0c01386

El Fewaty, N.H., El Sayed, A.M., Hafez, R.S.: Synthesis, structural and optical properties of tin oxide nanoparticles and its CMC/PEG–PVA nanocomposite films. Polym. Sci. Series A **58**, 1004–1016 (2016). https://doi.org/10.1134/S0965545X16060055

El Sayed, A.M., El-Gamal, S., Morsi, W.M., Mohammed, Gh.: Effect of PVA and copper oxide nanoparticles on the structural, optical, and electrical properties of carboxymethyl cellulose films. J. Mater. Sci. **50**, 4717–4728 (2015). https://doi.org/10.1007/s10853-015-9023-z

Elashmawi, I.S., Al-Muntaser, A.A.: Influence of Co_3O_4 nanoparticles on the optical, and electrical properties of CMC/PAM polymer: combined FTIR/DFT study. J. Inorg. Organomet. Polym. Mater. **31**, 2682–2690 (2021). https://doi.org/10.1007/s10904-021-01956-9

El-Gamal, S., El Sayed, A.M.: Physical properties of the organic polymeric blend (PVA/PAM) modified with MgO nanofillers. J. Compos. Mater. **53**(20), 2831–2847 (2019). https://doi.org/10.1177/0021998319840802

El-Sayed, S., Mahmoud, K.H., Fatah, A.A., Hassen, A.: DSC, TGA and dielectric properties of carboxymethyl cellulose/polyvinyl alcohol blends. Phys. B **406**, 4068–4076 (2011). https://doi.org/10.1016/j.physb.2011.07.050

Ibrahim, A.M.M., Elfadl, A.A., Sayed, A.M.E., Ibrahim, I.M.: Improving the optical, dielectric properties and antimicrobial activity of chitosan–PEO by GO/MWCNTs: nanocomposites for energy storage and food packaging applications. Polymer **267**, 125650 (2023). https://doi.org/10.1016/j.polymer.2022.125650

Jing, X., Chen, L., Li, Y., Yin, H., Chen, J., Su, M., Liu, F., Abdiryim, T., Xu, F., You, J., Liu, X.: Synergistic effect between 0D CQDs and 2D MXene to enhance the photothermal conversion of hydrogel evaporators for efficient solar water evaporation, photothermal sensing and electricity generation. Small **20**(50), 2405587 (2024). https://doi.org/10.1002/smll.202405587

Kumar, P., Kumar, H., Chand, S., Jain, S.C., Kumar, V., Kumar, V., Pant, R.P., Tandon, R.P.: Effect of CoFe magnetic nanoparticles on the hole transport in poly(2-methoxy, 5-(2-ethylhexiloxy)

1,4-phenylenevinylene). J. Phys. D Appl. Phys. **41**(18), 185104 (2008). https://doi.org/10.1088/0022-3727/41/18/185104

Kurtan, U., Sahinturk, U., Aydın, H., Dursun, D., Baykal, A.: CoFe nanoparticles in carbon nanofibers as an electrode for ultra-stable supercapacitor. J. Inorg. Organomet. Polym. Mater. **30**, 3608–3616 (2020). https://doi.org/10.1007/s10904-020-01524-7

Lefay, C., Guillaneuf, Y.: Recyclable/degradable materials via the insertion of labile/cleavable bonds using a comonomer approach. Prog. Polym. Sci. **147**, 101764 (2023). https://doi.org/10.1016/j.progpolymsci.2023.101764

Li, T., Li, B., Ji, Y., Wang, L.: Luminescent and UV-shielding ZnO quantum dots/carboxymethylcellulose sodium nanocomposite polymer films. Polymers **10**, 1112 (2018). https://doi.org/10.3390/polym10101112

Li, Y., Miao, R., Yang, Y., Han, L., Han, Q.: A zinc-ion battery-type self-powered strain sensing system by using a high-performance ionic hydrogel. Soft Matter **19**, 8022–8032 (2023a). https://doi.org/10.1039/D3SM00993A

Li, J.-X., Yang, H., Gu, R.-H., Dong, Y.-H., Cai, Y.-W., Zhao, Q., Chen, Y., Huang, M.: Fabrication of antibacterial Fe^{3+}-carboxymethylcellulose-polyacrylamide-Ag nanoparticles hydrogel coating for urinary catheters. Colloid Surf. A **672**, 131680 (2023b). https://doi.org/10.1016/j.colsurfa.2023.131680

Li, G., Shan, Y., Nie, W., Sun, Y., Su, L., Mu, W., Qu, Z., Yang, T., Wang, Q.: Application of carboxymethyl cellulose sodium (CMC–Na) in maize–wheat cropping system (MWCS) in coastal saline-alkali soil. Sci. Total. Environ. **912**, 169214 (2024a). https://doi.org/10.1016/j.scitotenv.2023.169214

Li, W., Li, S.-M., Kang, M.-C., Xiong, X., Wang, P., Tao, L.-Q.: Multi-characteristic tannic acid-reinforced polyacrylamide/sodium carboxymethyl cellulose ionic hydrogel strain sensor for human-machine interaction. Int. J. Biol. Macromol. **254**, 127434 (2024b). https://doi.org/10.1016/j.ijbiomac.2023.127434

Mahmoud, W.E., Al-Ghamdi, A.A.: The influence of vanadium pentoxide on the structure and dielectric properties of poly(vinyl alcohol). Polym. Int. **59**, 1282–1288 (2010). https://doi.org/10.1002/pi.2866

Morsi, M.A., El-Khodary, S.A., Rajeh, A.: Enhancement of the optical, thermal and electrical properties of PEO/PAM:Li polymer electrolyte films doped with Ag nanoparticles. Physica B **539**, 88–96 (2018). https://doi.org/10.1016/j.physb.2018.04.009

Morsi, M.A., Asnag, G.M., Rajeh, A., Awwad, N.S.: Nd:YAG nanosecond laser induced growth of Au nanoparticles within CMC/PVA matrix: multifunctional nanocomposites with tunable optical and electrical properties. Compos. Commun. **24**, 100662 (2021). https://doi.org/10.1016/j.coco.2021.100662

Morsi, M.A., Abdelrazek, E.M., Ramadan, R.M., Elashmawi, I.S., Rajeh, A.: Structural, optical, mechanical, and dielectric properties studies of carboxymethyl cellulose/polyacrylamide/lithium titanate nanocomposites films as an application in energy storage devices. Polym. Test. **114**, 107705 (2022). https://doi.org/10.1016/j.polymertesting.2022.107705

Pathak, R., Punetha, M., Bhatt, S., Pillai, S.A., Dhapola, P.S., Punetha, V.D.: Organic and inorganic nanofillers for polymer nanocomposit5es: trends, opportunities, and challenges. Adv. Funct. Polym. Nanocomp. (2024). https://doi.org/10.1016/B978-0-443-18860-2.00003-7

Qian, W., Jia, S., Yu, P., Li, K., Li, M., Lan, J., Lin, Y.-H., Yang, X.: Highly stretchable, low-hysteresis, and antifreeze hydrogel for low-grade thermal energy harvesting in ionic thermoelectric supercapacitors. Mater. Today Phys. **49**, 101589 (2024). https://doi.org/10.1016/j.mtphys.2024.101589

Ragab, H.M., Rajeh, A.: Structural, thermal, optical and conductive properties of PAM/PVA polymer composite doped with Ag nanoparticles for electrochemical application. J. Mater. Sci. Mater. Electron. **31**, 16780–16792 (2020). https://doi.org/10.1007/s10854-020-04233-6

Roheen, T., Ramzan, R., Nadeem, M., Atif, F.A., Munir, M., Qureshi, T.M.: Synthesis and characterization of CMC/PAM-Amy hydrogel and its efficacy in Apple juice clarification. Processes **12**, 2264 (2024). https://doi.org/10.3390/pr12102264

Steudel, A., Friedrich, F., Lieske, W., Baille, W., Konig, D., Schuhmann, R., Emmerich, K.: Simultaneous thermal analysis of cationic, nonionic and anionic polyacrylamide. Heliyon **5**, e02973 (2019). https://doi.org/10.1016/j.heliyon.2019.e02973

Sultan, M., Taha, G.: Sustained-release nitrogen fertilizer delivery systems based on carboxymethyl cellulose-grafted polyacrylamide: swelling and release kinetics. Int. J. Biol. Macromol. **266**, 131184 (2024). https://doi.org/10.1016/j.ijbiomac.2024.131184

Wan, G., Luo, Y., Wu, L., Wang, G.: The fabrication and high-efficiency electromagnetic wave absorption performance of CoFe/C core-shell structured nanocomposites. Nanoscale Res. Lett. **13**, 68 (2018). https://doi.org/10.1186/s11671-018-2474-9

Wang, L., Xu, M., Shi, B., Li, B.: Flame retardance and smoke suppression of CFA/APP/LDHs/EVA composite. Appl. Sci. **6**, 255 (2016). https://doi.org/10.3390/app6090255

Wang, L., Zhang, M., Zhou, B.: Thermal stability, com bustion behavior, and mechanical property in a flame-retardant polypropylene system. Appl. Sci. **7**, 55 (2017). https://doi.org/10.3390/app7010055

Wang, S., Kong, M., Li, W., Yi, E., Wang, Y., Shen, M., Liu, H., Ren, S., Guo, Y., Zhang, J.: Carboxymethyl cellulose/polyacrylamide/Fe_3O_4 magnetic ion imprinting biosorbent for removal and recovery of La^{3+}. ACS Omega **8**, 37374–37383 (2023). https://doi.org/10.1021/acsomega.3c05192

Wu, W., Feng, W., Yu, Y., Li, L., Lu, M., Qian, G., Chen, C., Min, D.: Highly sensitive MXene-enhanced polyacrylamide/ carboxymethyl cellulose double-network hydrogels with wide operation range for wearable electronics. Ind. Crops Prod. **214**, 118573 (2024). https://doi.org/10.1016/j.indcrop.2024.118573

Xu, Y., Sun, S., Maimaitiyiming, X.: High tensile poly(vinyl alcohol)/Carboxymethyl cellulose sodium/Polyacrylamide/Borax dual network hydrogel for lifting heavy weight and multi-functional sensors. Cellulose **30**, 11721–11736 (2023). https://doi.org/10.1007/s10570-023-05548-3

Yang, S., Wang, L., Yue, S., Lu, Y., He, J., Zhao, D.: Influence of reduction temperature on composition, particle size, and magnetic properties of CoFe alloy nanomaterials derived from layereddouble hydroxides precursors. Dalton Trans. **43**, 8254–8260 (2014). https://doi.org/10.1039/C4DT00137K

Yang, P., Song, Y., Sun, J., Wei, J., Li, S., Guo, X., Liu, C., Shen, C.: Carboxymethyl cellulose and metal-organic frameworks immobilized into polyacrylamide hydrogel for ultrahigh efficient and selective adsorption U (VI) from seawater. Int. J. Biol. Macromol. **266**, 130996 (2024). https://doi.org/10.1016/j.ijbiomac.2024.130996

Yu, B., Zhang, J., Gao, Z., Qi, X., Liu, B., Yang, J.: Stabilizing the Si/C blend anode by a multifunctional ternary composite binder. Mater. Lett. **373**, 137072 (2024). https://doi.org/10.1016/j.matlet.2024.137072